AGU PUBLICATIONS

JGR

Journal of Geophysical Research: Solid Earth

RESEARCH ARTICLE
10.1002/2015JB011998

Key Points:
- Slip rates on creeping section of San Andreas Fault vary over time
- Variation observed with repeating earthquakes confirmed with satellite geodesy
- Slip rates in some sections of the fault appear to vary in a cyclical manner

Supporting Information:
- Texts S1–S4, Figures S1–S4, and Table S4
- Figure S2.1
- Figure S2.2
- Figure S3

Correspondence to:
R. C. Turner,
rturner@seismo.berkeley.edu

Citation:
Turner, R. C., M. Shirzaei, R. M. Nadeau, and R. Bürgmann (2015), Slow and Go: Pulsing slip rates on the creeping section of the San Andreas Fault, *J. Geophys. Res. Solid Earth*, *120*, doi:10.1002/2015JB011998.

Received 1 MAR 2015
Accepted 1 JUL 2015
Accepted article online 14 JUL 2015

Slow and Go: Pulsing slip rates on the creeping section of the San Andreas Fault

Ryan C. Turner[1], Manoochehr Shirzaei[2], Robert M. Nadeau[1], and Roland Bürgmann[1,3]

[1]Berkeley Seismological Laboratory, University of California, Berkeley, California, USA, [2]School of Earth and Space Exploration, Arizona State University, Tempe, Arizona, USA, [3]Department of Earth and Planetary Science, University of California, Berkeley, California, USA

Abstract Rising and falling slip rates on the creeping section of the San Andreas Fault have been inferred from variations of recurrence intervals of characteristically repeating microearthquakes, but this observation has not previously been confirmed using modern geodetic data. Here we report on observations of this "pulsing" slip obtained from advanced multitemporal interferometric synthetic aperture radar (InSAR) data, confirmed using continuous GPS sites of the Plate Boundary Observatory. The surface deformation time series show a strong correlation to the previously documented slip rate variations derived from repeating earthquakes on the fault interface, at various spatial and temporal scales. Time series and spectral analyses of repeating earthquake and InSAR data reveal a quasiperiodic pulsing with a roughly 2 year period along some sections of the fault, with the earthquakes on the fault interface lagging behind the far-field deformation by about 6 months. This suggests a temporal delay between the pulsing crustal strain generated by deep-seated shear and the time-variable slip on the shallow fault interface, and that at least in some places this process may be cyclical. There exist potential impacts for time-dependent seismic hazard forecasting in California and, as it becomes better validated in the richly instrumented natural laboratory of the central San Andreas Fault, the process used here will be even more helpful in characterizing hazard and fault zone rheology in areas without California's geodetic infrastructure.

1. Introduction

Along creeping sections of the San Andreas and other faults, small asperities in the fault zone load and fail in characteristically repeating earthquake sequences (REQs), driven by aseismic creep on the surrounding fault plane [*Nadeau and McEvilly*, 1999, 2004]. These asperities represent less than 1% of the fault surface and do not contribute significantly to interplate coupling so they do not have a significant influence on slip rates. By identifying these sequences in the seismicity catalog using the cross correlation of their nearly identical waveforms and then using the empirical scaling relationship between moment magnitude and fault slip developed by *Nadeau and Johnson* [1998], we can translate these event recurrences into a measurement of subsurface fault creep. These natural creepmeters in the seismogenic zone can then be used to study time-dependent behavior on the fault interface [*Nadeau and McEvilly*, 2004]. We will show here that this time-dependent behavior is also observable with modern satellite-based geodesy, potentially making it possible to apply these techniques in less richly instrumented areas of the world.

The central creeping section of the San Andreas Fault (CSAF) extends from the San Juan Bautista transition zone in the northwest to the Parkfield transition zone in the southeast, where creeping ends and locked fault segments begin (Figure 1). The rupture zones of the great 1857 Fort Tejon and 1906 San Francisco earthquakes adjoin the CSAF to the south and north, respectively. Long studied using geodetic methods, the long-term surface slip rates of the CSAF are constrained by GPS and alignment arrays to reach up to 33.6 ± 1 mm yr at ± 35 km from the fault [*Titus et al.*, 2006], with accelerations near the transition zones due to the afterslip from large events such as the 1989 Loma Prieta [*Schaff et al.*, 1998] and 2004 Parkfield [e.g., *Freed*, 2007] earthquakes. *Nadeau and McEvilly* [2004] used slip data inferred from repeating earthquakes to describe a "pulsing," or rising and falling of the CSAF slip rate. Along some parts of the fault, the inferred slip rate at seismogenic depths can vary from the average rate by 100% or more on a two to three year cycle. While the pulsing slip rates are partly confirmed by surface creepmeter measurements [*Nadeau and McEvilly*, 2004], and while further work in California, Japan, and Taiwan has justified the use of repeating earthquakes for quantifying long-term slip rates [e.g., *Chen et al.*, 2007] and accelerated postseismic afterslip [e.g., *Uchida and Matsuzawa*, 2013; *Templeton et al.*, 2009], there has been

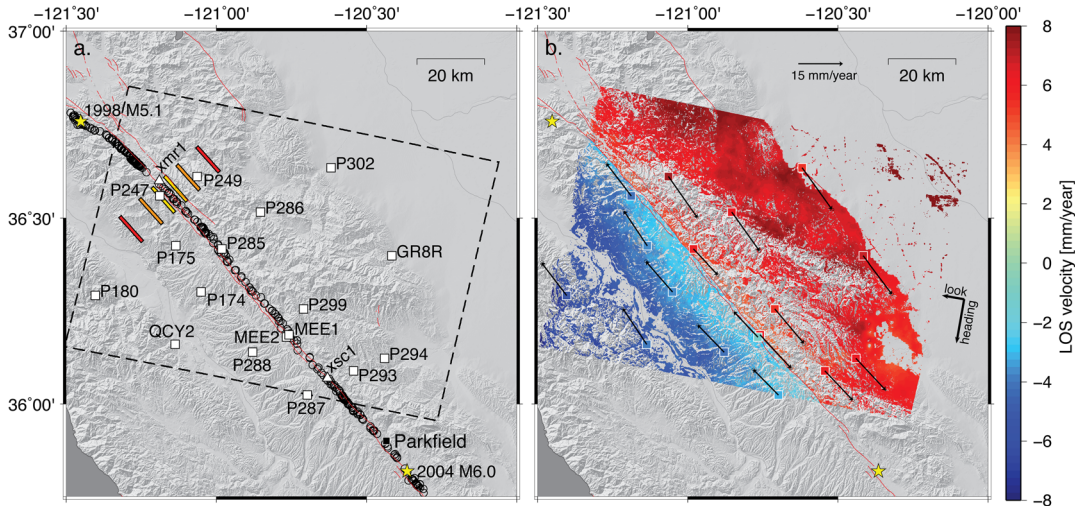

Figure 1. Study area along the CSAF. Active faults are shown in red [*U.S. Geological Survey and California Geological Survey*, 2006]. Stars mark the epicenter of the *M*5.1 1998 San Juan Bautista earthquake in the northwest and the northwest end of the *M*6 2004 Parkfield rupture in the southeast, roughly bounding the CSAF. (a) The yellow, orange, and red boxes represent 1 by 10 km example near-, middle-, and far-field zones (2–3, 7–8, and 15–16 km distance, respectively) where InSAR data are averaged to compare with slip inferred from nearby repeating earthquakes. The black circles show the locations of repeating earthquakes located along the fault interface. The white squares mark the locations of PBO continuous GPS sites and the two triangles mark the creepmeters in the study area, as labeled. The dashed rectangle marks the edge of the descending InSAR data set (ERS and Envisat) used in this study. (b) Colors indicate the linear line-of-sight (LOS) velocity from combined ERS and Envisat InSAR data (2006 to July 2010 shown here to better compare with the timeframe of available GPS data). Squares indicate the permanent GPS stations from Figure 1a, colored by their 3-D velocity projected into InSAR LOS direction on the same scale as the surrounding InSAR data and calibrated to match the InSAR velocity in the area surrounding P174 (see section 2.4 below). Arrows with 95% confidence ellipses show relative long-term horizontal velocity, scaled as indicated. The arrows in the upper right indicate the heading and look angle of the satellite tracks.

no satisfactory confirmation of shorter-term rate variations by geodetic methods. We will show that the spatial distribution of GPS instrumentation and the temporal resolution of previous interferometric synthetic aperture radar (InSAR) studies are to blame for this lack of confirmation.

In this study, after using GPS to corroborate a 7 year long InSAR time series (with ~6.5 scenes per year on average), we compare the CSAF slip rate variations derived from repeating earthquakes to the surface displacement time series from InSAR to find well correlated but phase-shifted periodic behavior in both data sets.

2. Data, Processing, and Validation

2.1. Slip Data From Repeating Earthquakes

The earthquake waveform data, spanning from 1984 to October 2011, comes from the Northern California Earthquake Data Center. The Northern California Seismic Network (NCSN) catalog has been searched for repeating earthquakes using cross correlation and spectral coherence methods to characterize waveform similarity between pairs of earthquakes after the method of *Nadeau and McEvilly* [2004]. When pairs of similar events are discovered, they are grouped together with other nearly identical pairs into repeating earthquake sequences, inferred to represent repeated failure of a discrete location on the fault [*Nadeau and McEvilly*, 1997]. The resulting catalog of repeating earthquakes spans the entire length of the CSAF, from the Loma Prieta aftershock region in the northwest [*Turner et al.*, 2013] through the Parkfield transition zone in the southeast. Along strike, 20–30 km beyond these transition zones, no repeating earthquakes are found, consistent with the absence of observed surface creep in these regions.

Each individual event in a repeating earthquake sequence corresponds to a specific amount of slip, given by the empirical scaling relationship

$$d_i = 10^{\alpha} M_0^{\beta},$$

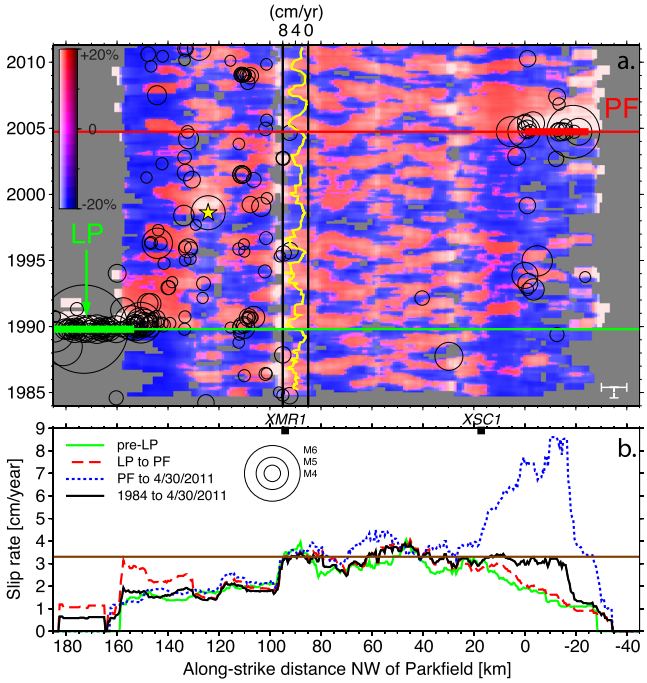

Figure 2. Changes in creep rate along CSAF from repeating earthquakes. (a) The slip rate, in percent difference from the average long-term rate, plotted along the entire length of the CSAF at 0.5 km increments, as it evolves through time. Gray indicates a lack of data (area searched but no repeating earthquake sequences found) while red and blue indicate slip rates at least 20% higher or lower than the long-term average at that location (shown in Figure 2b), respectively. White indicates higher uncertainty associated with fewer repeating earthquake sequences or with rapidly changing rates as in *Nadeau and McEvilly* [2004]. Smoothing along the fault uses a 10 km window along strike and a 0.8 year temporal smoothing window with values plotted at the end of the time window to provide a causal representation. White bars at the lower right show the spatial and temporal smoothing windows used. The Loma Prieta (LP) and Parkfield (PF) earthquakes are indicated by green and red lines respectively, thick for the extent of the rupture and thin along strike to indicate the temporal position of the event. All earthquakes along the fault with a magnitude greater than 3.5 are indicated by black circles, scaled to magnitude as shown in Figure 2b. The yellow highlighted slip rate history (given in absolute terms) in the section from 85 to 95 km NW of PF appears especially periodic and is described in more detail in section 3.2. (b) Average slip rate inferred from repeating earthquakes along the fault is shown for four periods. Slip rates before the Loma Prieta earthquake (pre-LP) are shown in solid green, between Loma Prieta and Parkfield (LP to PF) with red dashes, Parkfiled through April 2011 (PF to 30 April 2011) with blue dots, and the entire catalog from 1984 to April 2011 (1984—30 April 2011) in solid black. The straight brown line represents the long-term slip rate to be accommodated (here we use 33 ± 3 mm/yr [*Ryder and Bürgmann*, 2008]). The position "0" along strike aligns with the northwest end of the Parkfield rupture (PF). As in Figure 2a smoothing along the fault uses a 10 km long moving window, with data plotted at the center of the window each half kilometer along strike. Along-strike locations of the Melendy Ranch and Slack Canyon creepmeters (XMR1 and XSC1, respectively) are also shown.

where d_i is slip in centimeter and M_0 is seismic moment in dyne cm, inferred from NCSN preferred magnitudes (M_p) using the empirical relationship $log(M_0) = 1.6M_p + 15.8$ [*Wyss et al.*, 2004]. The slips (d_i) are interpreted to represent the cumulative slip on and surrounding the repeating earthquake patch over one seismic cycle. Values for α and β, used in this study are $\alpha = -2.36 \pm 0.2$ and $\beta = 0.17 \pm 0.001$ based on calibration with geodetic data at Parkfield [*Nadeau and Johnson*, 1998].

The CSAF does not slip uniformly and synchronously from one end of the creeping section to the other, so short-term slip histories differ along strike (Figure 2). To resolve variations of slip along strike while still allowing inclusion of enough repeating earthquake events to create a meaningful time series, we divide the fault into 10 km long segments. To obtain the cumulative displacement time series from such a subpopulation of repeating earthquake sequences, slip for each event is calculated, the slips were summed over the segment, and the total was then divided over the number of repeating earthquake sequences (rather than events) in that segment's population. In short, the repeating earthquake sequences were treated as an array of creepmeters, distributed throughout the segment, which were then averaged in space, making each event a step in the time series. An evenly sampled (0.1 year increment)

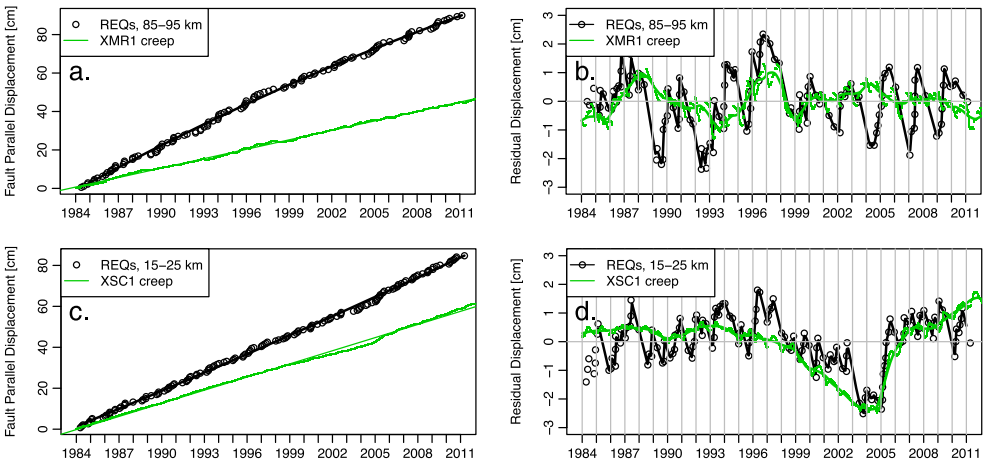

Figure 3. Repeating earthquakes and creepmeters. (a, c) Cumulative fault surface slip at creepmeters XMR1 and XSC1 (green lines, see locations in Figure 1a) compared to cumulative slip derived from repeating earthquakes from nearby 10 km long sections of the CSAF (85–95 km and 15–25 km from Parkfield, respectively) from 1984 to 2011 (black circles). (b, d) Detrended creepmeter data at XMR1 and XSC1, respectively, compared to the detrended slip derived from nearby repeating earthquakes.

displacement residual was computed using linear interpolation after removal of a linear trend representing the cumulative slip. The linear interpolation, required for processing the data as a regularly sampled data set rather than the irregular "sampling" represented by the individual earthquakes, simply fills the gaps between data points (earthquakes) with regularly sampled points representing the slope between adjacent points with no additional smoothing. The regular time series thus obtained allows for the clearest comparison between the various data sets. This technique was also employed for the InSAR data, as will be discussed in section 3.

One section of the fault, from 85 to 95 km NW of Parkfield in our fault-parallel coordinate system, appears to be particularly periodic throughout the $>$ 25 year observation period (Figure 2a). As this section is also over 50 km from the NW transition zone, thus minimizing the influence of large events, we examine this area in more detail and it is this segment that we highlight in the analysis in section 3.2.

2.2. Comparison of Creepmeter Time Series and Slip Inferred From Repeating Earthquakes

Comparisons between slip inferred from repeating earthquakes and creepmeter data help to confirm slip rates inferred from repeating earthquakes [*Nadeau and McEvilly*, 2004]. We examine the data from the two creepmeters in the study area and compare the surface creep time series to the repeating earthquake catalog. The creepmeter data, sampled at daily intervals throughout the time period, come from the U.S. Geological Survey (USGS) stations XMR1 at Melendy Ranch and XSC1 at Slack Canyon [*Burford*, 1988; *Bilham et al*., 2004]. Creepmeters consist of two piers separated by about 30 m and connected by a wire spanning the main fault trace of the San Andreas at an angle of roughly 30°. Comparisons of the creepmeter time series of surface slip with the rate variations inferred from nearby repeating earthquake data are shown in Figure 3. When we examine the residuals, we find a good correlation between the displacement given by the creepmeter data and that inferred from the repeating earthquakes, especially around the larger peaks in 1988 and 1997 for XMR1 and an acceleration of creep in late 2004 for XSC1. While the large excursions are visible in both data sets, qualitatively the creepmeter data appear as a smoothed version of the repeating earthquake time series. XMR1 indicates a significantly slower slip rate than do the repeating earthquakes at depth (16.4 versus 33.6 mm/yr) and appears to be located just up strike (northwest) from a large change in the long-term rate on the fault, while the bulk of the segment over which the REQs are averaged is in the higher-rate section to the southeast (Figure 2b). XSC1 also indicates slower displacement than the repeating earthquakes in the southeast (Figure 3, 21.4 mm versus 30.6 mm, respectively). While the creepmeter data provide direct near-fault measurement of the displacement across the fault at a single location, the repeating earthquakes sample slip along a 10 km long section of the fault across seismogenic depths and the physical dimensions of creepmeters

mean that they may not always capture the full motion across the fault, leading to measurements less than or equal to fault slip rates at depth [*Nadeau and McEvilly*, 2004, supplementary material]. Fault slip rate variations measured with short-aperture creepmeters may also be affected by shallow deformation transients due to soil expansion and contraction associated with rainfall and other nontectonic processes [*Bilham et al*., 2004].

2.3. InSAR and GPS Data and Processing

The InSAR time series are derived by applying the wavelet-based InSAR method [*Shirzaei*, 2013; *Shirzaei and Bürgmann*, 2013; *Shirzaei*, 2015] to a well-populated set of SAR data acquired by ERS (16 scenes) and Envisat (30 scenes) satellites in descending geometry from March 2003 to July 2010. We do not consider data collected by the ERS spacecraft from before 2003, as the temporal sampling during this period is too sparse to resolve rate variations along the fault [*Ryder and Bürgmann*, 2008]. We also do not use L-band data from the ALOS-1 satellite, which only collected $<$15 ascending acquisitions during ~4.5 years [*Tong et al*., 2013] or other ascending C-band data which, with a flight path almost parallel to the fault, captures only a small portion of the fault creep. To generate interferograms, we use the open source GMTSAR software [*Sandwell et al*., 2011]. The effects of topography are calculated and removed using a 90 m resolution Shuttle Radar Topography Mission digital elevation model (DEM) [*Farr et al*., 2007] and precise ephemeris data [*Franceschetti and Lanari*, 1999]. The effects of the residual orbital error and atmospheric error are reduced by use of various wavelet-based filters [*Shirzaei and Walter*, 2011; *Shirzaei and Bürgmann*, 2012; *Shirzaei*, 2013]. To correct the residual orbital error, we used a first-order polynomial. To reduce the spatially high-frequency noises such as DEM error, a filter based on Legendre polynomial wavelets of order one is applied. The topography-correlated atmospheric delay is estimated and removed using a filter based on Coiflet wavelets of order 5. Finally, the LOS time series is temporally low-pass filtered using continuous wavelet derivative of Gaussian of order 30. This analysis results in a time series of the surface deformation at more than 580,000 discrete locations distributed at varying distances across and along the fault. Figure 1b shows the average velocity in the line-of-sight direction of the InSAR acquisitions at each of these points from March 2003 to July 2010.

To estimate the InSAR uncertainties, we followed the concept of error propagation presented by *Mikhail and Ackermann* [1976]. In this approach the phase noise is estimated and then, through design matrices, is propagated to the InSAR time series, which allows estimating the InSAR uncertainties. For more details see equation 9 in *Shirzaei* [2013]. Shown uncertainties are the standard deviation, which represent internal consistencies of the InSAR and GPS data points and should not be directly compared. To make a direct comparison, one would need to estimate the relative weight between the two independent data sets, which is described as the variance factor in error analysis literature [*Mikhail and Ackermann*, 1976].

The GPS data are available from UNAVCO as part of the Plate Boundary Observatory, a component of EarthScope (PBO; data accessed at http://pbo.unavco.org/data/gps). The continuously operating PBO GPS stations used here were installed between 2006 and 2008. We use cleaned (level 2) station position data from the UNAVCO archive to obtain surface velocities and time series of displacement for each site (see supporting information Text S2 and Figures S2.1 and S2.2). We also compared the PBO data products (realized from a combination of processing results from Central Washington University, New Mexico Tech, and the Michigan Institute of Technology) with time series obtained from independent processing at NASA Jet Propulsion Laboratory and the University of Nevada, Reno. This comparison was done by finding the displacement time series between each GPS site and every other GPS site in the study area, removing the cumulative displacement, and visually inspecting the residuals for outliers (see supporting information Text S3 and Figure S3). The different processing solutions are in qualitative agreement in the long-term horizontal and vertical time series but there are instances of significant short-term variation between them (see baseline comparisons for P180-P301, P174-P286, and MEE1-MEE2 in Figure S3 for examples), a possible target for future study.

2.4. Validation of InSAR With GPS

To validate the InSAR time series, we average the InSAR points for each acquisition in a square box, roughly 200 m by 200 m, centered on each of the permanent GPS sites in the study area spanned by the InSAR data. This creates a 46-sample InSAR range-change time series in the immediate area around each station. We then make two projections of the GPS data into the InSAR line-of-sight (LOS) direction: one includes all three

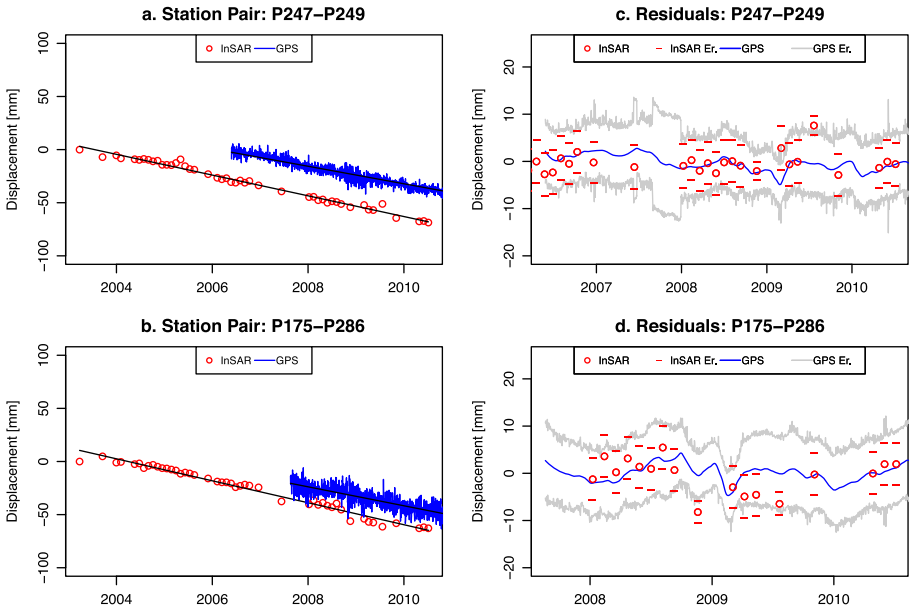

Figure 4. Comparison of GPS and InSAR time series. Shown here for two pairs of GPS stations near the XMR1 creepmeter (and the fault segment examined in further detail below, see Figure 1 for location) are the 3-D GPS and InSAR LOS displacement time series. Time series for all other station pairs are shown in supporting information Figures S2.1 and S2.2. (a, b) The displacement projected into LOS direction between two GPS sites is shown in blue and the displacement between the InSAR points in a roughly 200 by 200 m box around those same sites in red. Note that the two time series are vertically offset from one another for clarity and the linear trend of each (black lines) are in excellent agreement, as expected. (c, d) The same data with the linear trend removed, 1 sigma error bars added, and temporally cropped to highlight only the overlapping dates.

displacement components, north, east, and up, while a second includes only the more precise horizontal GPS components. The GPS data are aligned to the InSAR data by matching the LOS velocity at one site (P174) to the collocated InSAR velocity. The average LOS rates are shown in Figure 1b using all three GPS components and indicate general agreement between the long-term surface velocities obtained from the GPS and InSAR data. The result is similar using only the 2-D horizontal components projected into the InSAR LOS (RMS of 14.27 versus 14.35 for 3-D and 2-D LOS velocities compared to InSAR, respectively), confirming that the long-term deformation along the CSAF is dominated by horizontal motions.

The projections also allow for comparison of GPS and InSAR time series for each spatial baseline between pairs of GPS/InSAR sites. The GPS-measured and InSAR-measured displacement time series of a first site are subtracted from the corresponding motions of a second site to give the change with time in the InSAR LOS component of the baseline. Removing the simple, linear long-term trend from each time series, we can compare the residuals and find that the InSAR and GPS measurements generally fall within their common error at the times and locations where both data sets are available (see example in Figure 4 and results for all 3-D baseline time series in supporting information Figure S2.1). Comparing the 2-D and 3-D GPS data to the InSAR data, the InSAR tends to agree more closely with the 3-D GPS (see supporting information Figure S2.2 for 2-D baseline time series). This implies that in some areas there is a real time-dependent vertical signal and that signal is observable through InSAR. Significant work is currently being done examining the vertical component of the GPS time series including a number of recent publications [*Amos et al.*, 2014; *Argus et al.*, 2014; *Borsa et al.*, 2014] that examine the western U.S. in detail and find significant contributions from hydrological surface loads. Substantial vertical deformation can also result from poroelastic deformation in response to groundwater level in sedimentary basins [e.g., *Chaussard et al.*, 2014]. As we do not resolve a strong annual period in our analysis, we do not believe that such dominantly seasonal processes strongly affect our results.

While it would be preferable to compare the repeating earthquake slip residuals and GPS residuals directly, there is not an appropriate station pair with which to do so. The ideal station pair would form a 40 km baseline, centered on and perpendicular to the fault. Local variability is quite high, and even a few kilometers make a difference. For this reason, we are limited to comparing the GPS with the InSAR where both are available and then comparing the InSAR displacement to the slip from repeating earthquakes.

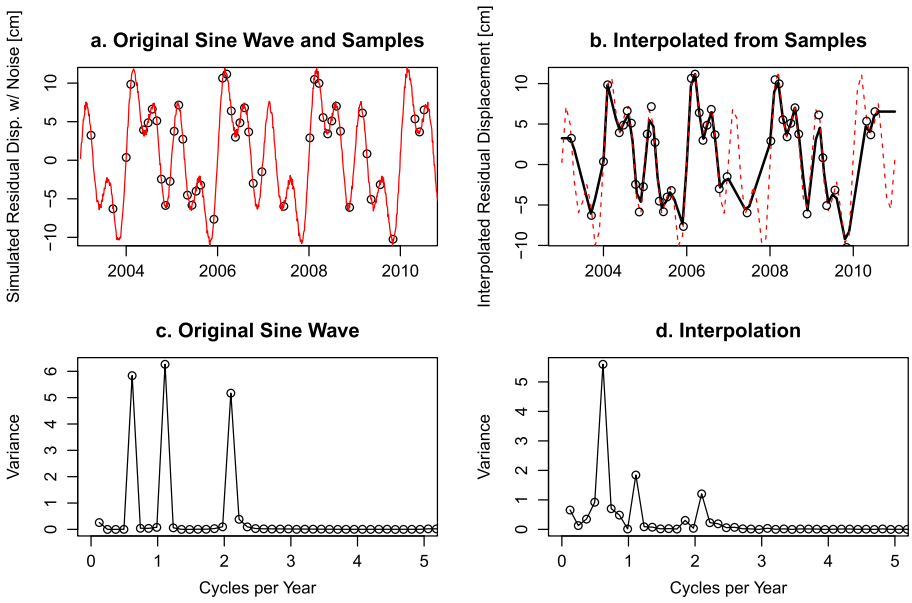

Figure 5. Results of test with synthetic data. (a) Original sine wave plotted in red with the locations of the samples chosen to correspond to the InSAR acquisition times in the real data marked by black circles. (b) Linear interpolation in black with locations of the samples from which the interpolation is made marked with black circles. Original sine wave in dashed red. (c, d) Spectral plots of the original continuous signal and interpolated data, respectively.

This illustrates one of the major benefits of the technique—the major part of the analysis presented here can be performed even in areas without the rich instrumentation of the Central San Andreas Fault.

3. Periodicity in Cross-Fault InSAR Time Series and Repeating Earthquakes

To look for periodicity in the InSAR and repeating earthquake data, we use spectral analysis to find the dominant frequency in the respective time series. While the repeating earthquakes directly probe variations in aseismic slip rate on the upper ~15 km of the CSAF, we examine temporal variations in

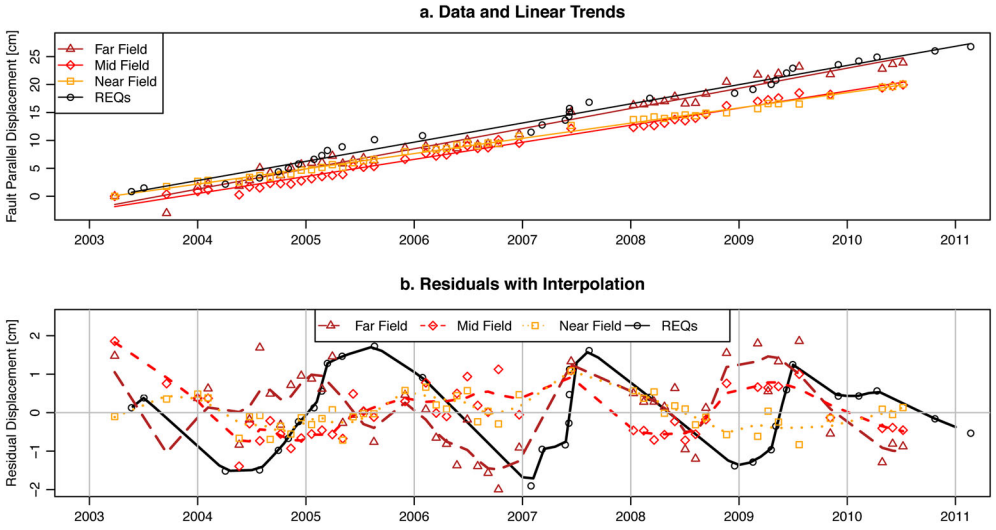

Figure 6. Example of time series comparison along 85 to 95 km distance from Parkfield. (a) The far-, middle-, and near-field InSAR series are shown with maroon triangles, red diamonds, and yellow squares, respectively. Repeating earthquakes are shown with black circles. The linear trend representing the long-term rate is also shown for each series. (b) The residuals, each shown with the same color and symbol as above. Linear interpolation also shown as solid or dashed lines as noted in the key. Further detailed below, the maximum cross-correlation coefficient for the far-field InSAR series and the repeating earthquake series is ~0.5 at a lag of about 6 months.

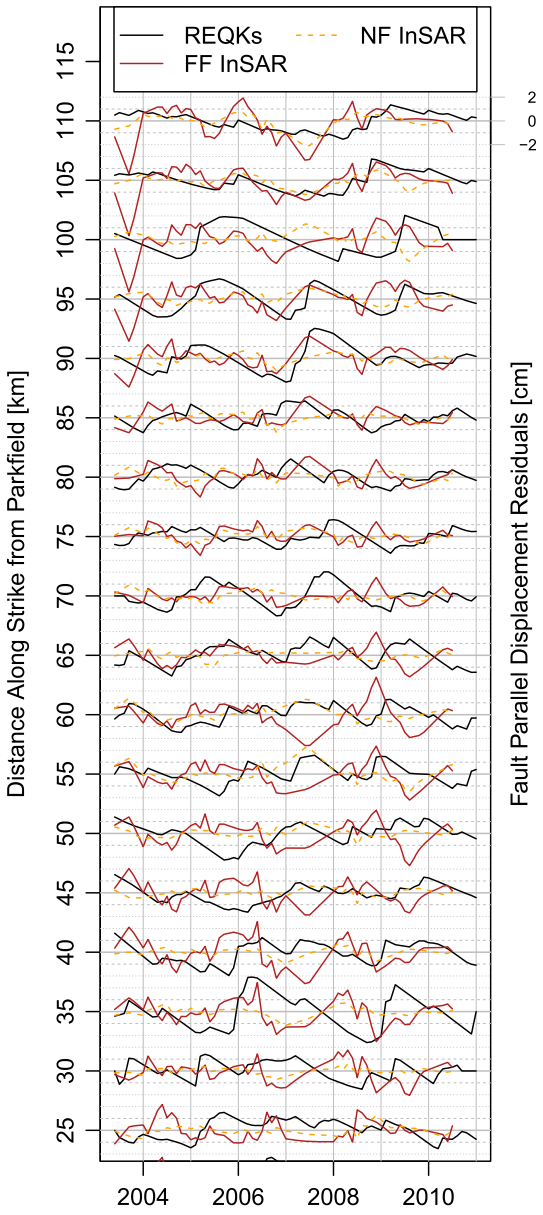

Figure 7. InSAR and repeating earthquakes, along strike. Each group of displacement residuals is a simplified version of Figure 6b (showing only repeating earthquakes (REQKs), far-field (FF), and near-field (NF) InSAR), plotted along strike to cover the CSAF spanned by the InSAR data. Because the spatial window is 10 km in width and the figure shows residuals at 5 km increments, it should be noted that each group shares 50% of its data with the group "above" and 50% with the group "below."

relative LOS motions of groups of InSAR points at varying distances from the fault to evaluate periodic behavior of cross-fault deformation. A spectral plot is an estimate of the spectral density of a signal. The plot relates the frequency of a signal to the variance of the signal contributed at that frequency.

In this case, the signals are the time series of the InSAR cross-fault motions and repeating earthquake data, linearly interpolated from the individual observations. By comparing the spectral plots of the two signals, we can detect periodicity in a quantitative manner. Before applying this technique to real data, the method was tested using a synthetic data set as described below.

3.1. Synthetic Tests

To ensure that our temporal sampling of the InSAR data is sufficient to reveal periodicities in the displacement rate variation, tests were conducted using synthetic data. Additionally, probabilistic "bootstrapping" tests were performed to evaluate the effect of noise and gaps in the data on the resulting spectral analysis.

A composite sine wave of known periods and amplitude was generated with the following equation,

$$y(t) = 5\sin\left(\frac{2\pi}{T_1}t\right) + 5\sin\left(\frac{2\pi}{T_2}t\right) + 5\sin\left(\frac{2\pi}{T_3}t\right) + 1.0w$$

where $y(t)$ is the synthetic displacement at time t in centimeters, $T_1 = 2$ years, $T_2 = 1$ year, and $T_3 = 0.5$ years are the assumed signal periods (corresponding to frequencies of one half, one, and two cycles per year,), t spans our ~7 year time interval in 0.01 year steps, and w corresponds to white noise with a variance of 1 cm. The synthetic data were then sampled at points corresponding to the dates of our InSAR time series (Figure 5a). This sampling was then linearly interpolated in the same fashion as our repeating earthquake and InSAR data (Figure 5b) to see if it is possible to recover the original periods in the synthetic time series (Figures 5c and 5d). Figure 5 shows that from the interpolated time series of just 46 observations spanning 7 years, we can easily pick out the 2 year signal (as well as periods up to 3 years, not shown). The shorter-period signals (12 months and 6 months) are also visible but are not as prominent in the spectral plot. In short, this test shows that we can indeed reconstruct the general features of the original signal with these methods.

To examine the effect of noise in the InSAR data, the original signal was generated and random noise with a variance of 2 cm added. As before, the resulting signal was then sampled at the times of the available InSAR observations, linearly interpolated and spectrally analyzed. To generate an ensemble, this process was then repeated 500 times (with different random noise at each iteration) to allow an approximation of

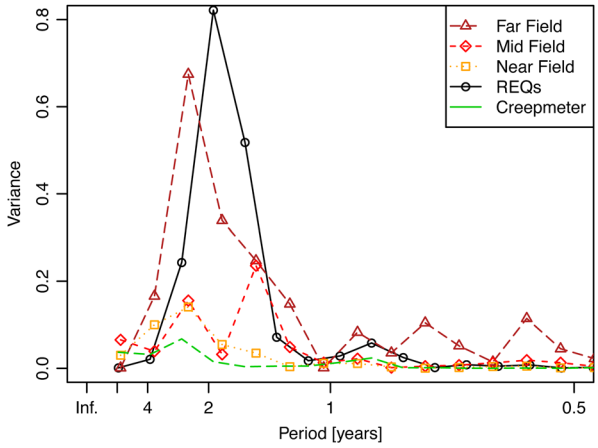

Figure 8. Spectral plots: The spectral plots of the REQ and InSAR time series from the 85–95 km distance segment. The far-field InSAR and repeating earthquakes both show a dominant period of 2–2.5 years. A similar period is visible in the middle- and near-field InSARs but is of significantly lower variance.

the probability density function (PDF) of the estimated dominant frequencies. This PDF was then used to investigate the effect of observational noise on the spectral analysis.

To examine the effect of gaps in the data, the original signal is again generated but with no random noise added. Rather, the signal is randomly sampled, linearly interpolated, and spectrally analyzed. To generate an ensemble, the random sampling step is repeated 500 times, which allows approximating the PDF of the estimated dominant frequencies. As above, this PDF is used to investigate the effect of data gaps on the spectral analysis.

The presence of random error in the data causes 27%, 8%, and 51% error in estimating periods of 2, 1, and 0.5 years, respectively. The corresponding results for the case of data gaps are, 20%, 11%, and 6% errors, respectively. We note that these results are unique to the investigated case here, but the approach is general and can be applied elsewhere.

3.2. Comparing InSAR and Fault Slip Data From Repeating Earthquakes

To compare the data sets, a group of time series are created for a given fault segment. InSAR data points in 1 km wide, 10 km long boxes are selected at three perpendicular distances from the fault segment (near, middle, and far fields corresponding to 2, 7, and 20 km from the SAF) and the data in these boxes are averaged and differenced with an identical box on the opposite side of the fault (Figure 1). Examining the surface deformation at different distances from the fault can be thought of as imaging the behavior on the fault interface at roughly corresponding depths. The distances used here correspond to the top, bottom, and below the seismogenic zone where we see the repeating earthquakes. This differential LOS measurement is then rotated into a fault-parallel orientation (assuming horizontal fault-parallel motions only) and the 138 discrete observations (46 observations at three across-fault distances) are interpolated in the same linear fashion as the repeating earthquakes after removing the long-term trend to create a time series that is regularly sampled at 0.1 year increments (Figure 6a). As mentioned in section 2.1, we have chosen the fault segment from 85 to 95 km to illustrate this analysis, as the repeating earthquake rates appear particularly periodic (Figure 2) and are not affected by slip transients associated with afterslip from recent large earthquakes such as the 2004 Parkfield and 1989 Loma Prieta events. Figure 7 shows comparisons of detrended time series of slip inferred from the repeating earthquakes and middle- and far-field fault-parallel displacements from the InSAR data as a function of distance along the high slip rate section of the CSAF spanned by the InSAR data.

3.3. Spectral Analysis and Cross Correlation of Periodic Displacements

Having generally confirmed the repeating earthquake (section 2.2) and InSAR time series (section 2.4), statistical analyses of correlation, phase, and spectra reveal several features. The spectral plots (described in section 3) of the time series along the 85–95 km distance segment reveal a dominant period of approximately 2 years (or ~0.5 cycles per year) for both the repeating earthquakes and the InSAR data (Figure 8).

The cross-correlation function (CCF) is a measure of the similarity of two waveforms when a time-lag or phase shift is added to one of them. The CCF of the repeating earthquakes and the InSAR time series at varying distances from the fault reveals correlations and anticorrelations with the near field and midfield that are somewhat difficult to interpret but relatively strong correlations with the far-field InSAR in both positive and negative lag—a product of their shared periodicity (Figure 9). The CCF of the repeating earthquakes with the far-field InSAR indicates a phase shift of about 6 months, and inspection of Figure 6b shows that the far-field deformation appears to lead the slip derived from the repeating earthquakes.

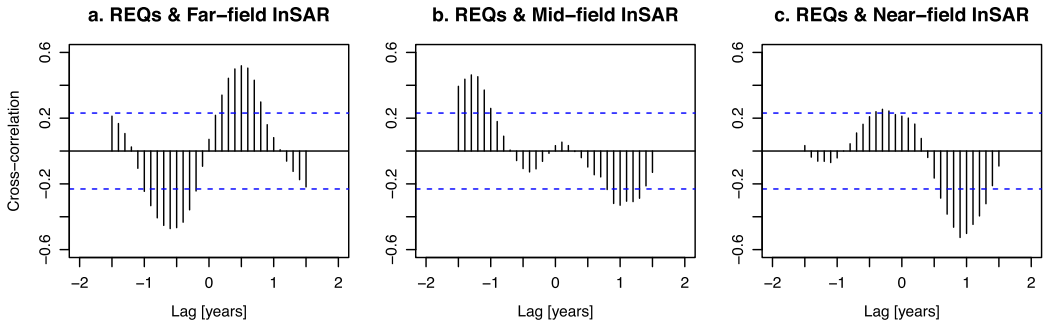

Figure 9. CCF: (a–c) The cross-correlation functions of the repeating earthquakes with the far-, middle-, and near-field InSAR time series reveal correlations between each with the far field showing strong (~0.5) correlation to the repeating earthquakes in both positive and negative lags, a product of their shared periodicity. The CCF can be conceptualized as the fit of the curve representing the given InSAR time series in Figure 7b with the curve representing the repeating earthquake-based time series as the former is moved forward and backward in time with respect to the latter. With uncorrelated white noise, we would expect ~5% of the values to fall outside of the dashed lines while here we see cross correlations greater than 0.5 at points in each series.

4. Discussion

The rising and falling slip rates on the CSAF as observed from repeating earthquakes appear correlated with episodic deformation measured on the surface with InSAR. In the example considered in the spectral analysis for a section 85–95 km northwest of Parkfield, the surface deformation rate in the far field (at ~15 km distance from the fault) shows a strong correlation with the slip rate derived from repeating earthquakes on the fault interface. Analysis along that section of the fault reveals quasiperiodic pulsing of 2 to 2 1/2 years in both data sets, with the earthquakes on the fault interface lagging about 6 months behind the far-field deformation. It should be noted that while the repeating earthquakes are on the fault itself and are in that sense "near field," their behavior most directly maps to surface displacements at a distance from the fault approximately equal to their depth. Slip behavior in the uppermost several hundred meters of the fault, the region that most directly maps to our near-field InSAR data, may be quite decoupled from slip at seismogenic depths. While different in the details because of significant variation along and across strike, similar behavior is seen along the remainder of the high slip rate section of the CSAF (Figure 7).

Our favored interpretation is that this 6 month lag represents the local accumulation of strain in the crust as the plates move in the regional scale. More specifically, the lag is the time needed to load repeating earthquake asperities on the segment and cause them to fail as part of a prolonged slow-slip event. The rising and falling rates might then indicate episodic deep aseismic shear, perhaps migrating in pulses from depth—a notion worthy of future study. While the signal in our data is decreasingly clear with proximity to the fault as surface deformation begins to dominate, perhaps the next generation of spacecraft with their vastly improved temporal resolution will be better able to image a lag that increases with proximity to the fault.

In this work, the repeating earthquakes (found between 2 and 8 km in depth, throughout the seismogenic zone in the central part of CSAF) are not discretized with respect to depth due to the relatively sparse data. Some investigation has been done despite this by dividing the REQs at 5.15 km depth (50% above and 50% below, by number). There was no resolvable difference in the long-term rate (1984–2004) but there was some difference after the Parkfield earthquake in 2004. This may have been resolvable because of the large acceleration of REQs in the postseismic afterslip period (denser data) but could also be explained by local variations. It is possible that there could be a resolvable difference if more data (repeating earthquake sequences) were available. In that regard, we have been very conservative in our identification of repeating earthquake sequences and it may be possible to lower the threshold a bit and densify the data sufficiently to discretize the events with respect to depth. With respect to the findings of this work, it would be particularly interesting to see a lag between the deeper and shallower events.

To examine the behavior of the entire CSAF and to better understand the possible correlation between the temporal variability of surface deformation and fault slip, a joint inversion of geodetic and repeating earthquake data for the spatiotemporal evolution of slip is the next logical step [*Shirzaei and Bürgmann*, 2013;

M. Khoshmanesh et al., Time-dependent model of aseismic slip on the central San Andreas Fault from InSAR time series and repeating earthquakes, submitted to *Journal of Geophysical Research Solid Earth*, in review, 2015].

5. Conclusions

We consider a 28 year catalog of repeating earthquakes that encompasses the entire creeping section of the CSAF with no repeating earthquakes found beyond the San Juan Bautista and Parkfield transition zones in the northwest and southeast, respectively. The pulsing behavior observed in the slip rates inferred from repeating earthquakes and noted by Nadeau and McEvilly in 2004 has persisted for the duration of the observation. Furthermore, the temporal variability of these slip rates is confirmed geodetically using 46 InSAR scenes spanning 7 years. The deformation rates observed in the InSAR time series, supported using continuous GPS stations in the region, also vary in time and appear to be spatially and temporally correlated with the slip on the fault. The deformation rates in the far field appear to lead the slip rates on the fault by about 6 months, implying that it takes some time to build elastic strain in the crust before that strain is relieved by accelerated slip on the fault. It is hoped that the InSAR techniques applied here can help to better characterize time-dependent behavior and fault zone rheology in regions that do not share California's excellent seismic and geodetic networks.

Acknowledgments

The authors wish to thank Naoki Uchida and the PBO field engineers of the Southwest Region for helpful discussions as well as the Associate Editor and two anonymous reviewers for comments that improved the manuscript. This work is supported through National Science Foundation grant EAR-0951430. Shirzaei was supported by National Science Foundation grants EAR-1357079 and EAR-0951430 and United States Geological Survey grant G13AP00040. This material is based on data services provided by UNAVCO through the GAGE Facility with support from the National Science Foundation (NSF) and National Aeronautics and Space Administration (NASA) under NSF cooperative agreement EAR-1261833. InSAR data comes from European Space Agency and UNAVCO archives. Waveform data provided by the Northern California Seismic Network, USGS, Menlo Park by way of the Northern California Earthquake Data Center at the Berkeley Seismological Laboratory (BSL). BSL contribution 2015-05.

References

Amos, C. B., P. Audet, W. C. Hammond, R. Burgmann, I. A. Johanson, and G. Blewitt (2014), Uplift and seismicity driven by groundwater depletion in central California, *Nature*, *509*(7501), 483–486.

Argus, D. F., Y. Fu, and F. W. Landerer (2014), Seasonal variation in total water storage in California inferred from GPS observations of vertical land motion, *Geophys. Res. Lett.*, *41*, 1971–1980, doi:10.1002/2014GL059570.

Bilham, R., N. Suszek, and S. Pinkney (2004), California creepmeters, *Seismol. Res. Lett.*, *75*(4), 481–492, doi:10.1785/gssrl.75.4.481.

Borsa, A. A., D. C. Agnew, and D. R. Cayan (2014), Ongoing drought-induced uplift in the western United States, *Science*, *345*(6204), 1587–1590.

Burford, R. O. (1988), Retardations in fault creep rates before local moderate earthquakes along the San Andreas fault system, central California, *Pure Appl. Geophys.*, *126*(2-4), 499–529, doi:10.1007/BF00879008.

Chaussard, E., R. Bürgmann, M. Shirzaei, E. J. Fielding, and B. Baker (2014), Predictability of hydraulic head changes and characterization of aquifer-system and fault properties from InSAR-derived ground deformation, *J. Geophys. Res. Solid Earth*, *119*, 6572–6590, doi:10.1002/2014JB011266.

Chen, K. H., R. M. Nadeau, and R.-J. Rau (2007), Towards a universal rule on the recurrence interval scaling of repeating earthquakes?, *Geophys. Res. Lett.*, *34*, L16308, doi:10.1029/2007GL030554.

Farr, T. G., et al. (2007), The Shuttle Radar Topography Mission, *Rev. Geophys.*, *45*, RG2004, doi:10.1029/2005RG000183.

Franceschetti, G., and R. Lanari (1999), *Synthetic Aperture Radar Processing*, *Electron. Eng. Syst. Ser.*, CRC Press, New York.

Freed, A. M. (2007), Afterslip (and only afterslip) following the 2004 Parkfield, California, earthquake, *Geophys. Res. Lett.*, *34*, L06312, doi:10.1029/2006GL029155.

Mikhail, E. M., and F. E. Ackermann (1976), *Observations and Least Squares*, *IEP Ser. Civ. Eng.*, Harper and Row, New York.

Nadeau, R. M., and L. R. Johnson (1998), Seismological studies at Parkfield VI: Moment release rates and estimates of source parameters for small repeating earthquakes, *Bull. Seismol. Soc. Am.*, *88*(3), 790–814.

Nadeau, R. M., and T. V. McEvilly (1997), Seimological studies at Parkfield V: Characteristic microearthquake sequences as fault-zone drilling targets, *Bull. Seismol. Soc. Am.*, *87*(6), 1463–1472.

Nadeau, R. M., and T. V. McEvilly (1999), Fault slip rates at depth from recurrence intervals of repeating microearthquakes, *Science*, *285*(5428), 718–721, doi:10.1126/science.285.5428.718.

Nadeau, R. M., and T. V. McEvilly (2004), Periodic pulsing of characteristic microearthquakes on the San Andreas fault, *Science*, *303*(5655), 220–222, doi:10.1126/science.1090353.

Ryder, I., and R. Bürgmann (2008), Spatial variations in slip deficit on the central San Andreas Fault from InSAR, *Geophys. J. Int.*, *175*(3), 837–852, doi:10.1111/j.1365-246X.2008.03938.x.

Sandwell, D., R. Mellors, X. Tong, M. Wei, and P. Wessel (2011), Open radar interferometry software for mapping surface deformation, *Eos Trans. AGU*, *92*(28), 234–234, doi:10.1029/2011EO280002.

Schaff, D. P., G. C. Beroza, and B. E. Shaw (1998), Postseismic response of repeating aftershocks, *Geophys. Res. Lett.*, *25*(24), 4549–4552, doi:10.1029/1998GL900192.

Shirzaei, M. (2013), A wavelet-based multitemporal DInSAR algorithm for monitoring ground surface motion, *IEEE Geosci. Remote Sens. Lett.*, *10*(3), 456–460, doi:10.1109/LGRS.2012.2208935.

Shirzaei, M. (2015), A seamless multitrack multitemporal InSAR algorithm, *Geochem. Geophys. Geosyst.*, *16*, 1656–1669, doi:10.1002/2015GC005759.

Shirzaei, M., and R. Bürgmann (2012), Topography correlated atmospheric delay correction in radar interferometry using wavelet transforms, *Geophys. Res. Lett.*, *39*, L01305, doi:10.1029/2011GL049971.

Shirzaei, M., and R. Bürgmann (2013), Time-dependent model of creep on the Hayward fault from joint inversion of 18 years of InSAR and surface creep data, *J. Geophys. Res. Solid Earth*, *118*, 1733–1746, doi:10.1002/jgrb.50149.

Shirzaei, M., and T. R. Walter (2011), Estimating the effect of satellite orbital error using wavelet-based robust regression applied to InSAR deformation data, *IEEE Trans. Geosci. Remote Sens.*, *49*(11), 4600–4605.

Templeton, D. C., R. M. Nadeau, and R. Bürgmann (2009), Distribution of postseismic slip on the Calaveras fault, California, following the 1984 M6.2 Morgan Hill earthquake, *Earth Planet. Sci. Lett.*, *277*(1–2), 1–8, doi:10.1016/j.epsl.2008.09.024.

Titus, S. J., C. DeMets, and B. Tikoff (2006), Thirty-five-year creep rates for the creeping segment of the San Andreas Fault and the effects of the 2004 Parkfield earthquake: Constraints from alignment arrays, continuous Global Positioning System, and creepmeters, *Bull. Seismol. Soc. Am.*, *96*(4B), S250–S268, doi:10.1785/0120050811.

Tong, X., D. T. Sandwell, and B. Smith-Konter (2013), High-resolution interseismic velocity data along the San Andreas Fault from GPS and InSAR, *J. Geophys. Res. Solid Earth*, *118*, 369–389, doi:10.1029/2012JB009442.

Turner, R. C., R. M. Nadeau, and R. Bürgmann (2013), Aseismic slip and fault interaction from repeating earthquakes in the Loma Prieta aftershock zone, *Geophys. Res. Lett.*, *40*, 1079–1083, doi:10.1002/grl.50212.

Uchida, N., and T. Matsuzawa (2013), Pre- and postseismic slow slip surrounding the 2011 Tohoku-oki earthquake rupture, *Earth Planet. Sci. Lett.*, *374*, 81–91, doi:10.1016/j.epsl.2013.05.021.

U.S. Geological Survey and California Geological Survey (2006), Quaternary fault and fold database for the United States. [Available at http//earthquakes.usgs.gov/regional/qfaults/ (Accessed 5 May 2010).]

Wyss, M., C. G. Sammis, R. M. Nadeau, and S. Wiemer (2004), Fractal dimension and b-value on creeping and locked patches of the San Andreas Fault near Parkfield, California, *Bull. Seismol. Soc. Am.*, *94*(2), 410–421, doi:10.1785/0120030054.